Nanoscale

RSC Publishing

PAPER

View Article Online
View Journal | View Issue

Published on 19 July 2013. Downloaded by Synchrotron Radiation Library on 25/11/2013 06:52:47.

Cite this: *Nanoscale*, 2013, **5**, 9181

Heterogeneous junction engineering on core–shell nanocatalysts boosts the dye-sensitized solar cell†

Chiun-Yi Wu,‡[a] Yu-Ting Liu,‡[b] Po-Chun Huang,[a] Tzy-Jiun Mark Luo,[c] Chih-Hao Lee,[ad] Yaw-Wen Yang,[d] Ten-Chin Wen,[e] Tsan-Yao Chen*[a] and Tsang-Lang Lin*[a]

Received 27th April 2013
Accepted 17th July 2013

DOI: 10.1039/c3nr02107f

www.rsc.org/nanoscale

In this study, we successfully manipulate the heterogeneous junction at Co_3O_4–Pt core–shell cathodic nanocatalysts (C/P CNCs) by controlling the core/shell ratios. Our results indicate the cobalt core atoms would inject their valence charge to the surface Pt atoms due to the presence of extensive lattice strain in the shell region. This charge injection accelerates the redox kinetics at the catalysts surface. Consequently, compared with that using Pt nanoparticle cathode, the C/P CNCs at an optimal Pt/Co atomic ratio of 1, improves the current density and the photovoltaic efficiency of dye-sensitized soar cell (DSSC) by ~36.3% and ~22.9%, respectively. By combining structure and electrochemical analysis, we systematically elucidate the effects of Pt/Co (shell/core) ratios, the interplay of Co atoms on the shell structures, and the redox activity of C/P CNCs on the DSSC performance. Hereby, this study provide mechanistic insights in developing electrocatalysts for DSSC with programmable performance and reduced Pt utilization.

Introduction

Dye-sensitized solar cell (DSSC) is one of the promising candidates for inexpensive, eco-friendly, and mass-productive photovoltaic technology.[1] Their counter electrode (CE) collects the photon-generated electrons from the external circuit to process the I_3^- reduction, thus regenerating the photon sensitizer at the anode to complete the redox cycle in the DSSC.[2–4] Conventional industrial approaches had shown that this cathode can be easily fabricated by coating the platinum layers (in the form of thin film or nanoparticles) on fluorine-doped tin oxide (FTO) conductive glass and flexible conducting polymers.[1,2] Although equipping it with a high performance anode and a platinized cathode allowed the DSSC to show compatible photovoltaic efficiency (~13.5%)[5] to that of commercialized photovoltaic devices, the availability and cost of noble metals have hindered their further development.[1] There are quite a few competitive techniques for photoelectrochemical devices; however, the only common consensus is to apply the low cost metal oxide or compound CE to the DSSC module.[3,4,6,7]

Hence, from considerations of chemical stability and cost-effectiveness it is imperative to develop a new class of catalyst that contains reduced Pt content yet provides improved redox reaction efficiency, sustained lifetime, and reduced manufacturing cost.[8] To achieve this goal, previous researches have chosen carbon materials and conducting organic polymers as cathodic nanocatalysts (CNCs) in DSSC.[9] Other studies found that inorganic compounds such as CoS, NiS, Cr_2O_3, and NiN can be employed as CNCs with the efficiency equivalent to the Pt nanoparticles (NPs).[10,11] Although these reports have successfully established the cost-effective strategies, the low chemical stability of organic/inorganic compounds in highly corrosive electrolytes may compromise their sustainability in a DSSC system.[12]

Based on the heterogeneous catalysis theory the specific surface area, the extent of heteroatomic intermixes, and the lattice strains in the shell region are the deciding factors in CNCs activity. These factors, according to the structural characterizations augmented by the first-principle density functional theory (DFT) calculations, offer a new mechanistic insight into atomistic surface chemistry with unprecedented details and consequently open the possibilities to optimize the photovoltaic efficiency of DSSC.[8,13–17]

[a]*Department of Engineering and System Science, National Tsing Hua University, Hsinchu 30013, Taiwan. E-mail: g9711531@oz.nthu.edu.tw; s9911542@m99.nthu.edu.tw; chencaeser@gmail.com; tllin@mx.nthu.edu.tw; chlee@mx.nthu.edu.tw; Fax: +886 3 5728445; Tel: +886 3 5742671*

[b]*Department of Environmental Science and Engineering, Tunghai University, Taichung, Taiwan. E-mail: ytliu@thu.edu.tw*

[c]*Department of Materials Science and Engineering, North Carolina State University, Raleigh, NC 27695, USA. E-mail: chencaeser@gmail.com; tluo@ncsu.edu*

[d]*National Synchrotron Radiation Research Center, Hsinchu 30076, Taiwan. E-mail: yang@nsrrc.org.tw*

[e]*Department of Chemical Engineering, National Cheng Kung University, Tainan 70101, Taiwan. E-mail: tcwen@mail.ncku.edu.tw*

† Electronic supplementary information (ESI) available: The SAXS data analysis, Pt and L3-edge XAS analysis, XRD analysis, and VB spectra of experiment samples are enclosed. Details procedure and scheme for synthesis the DSSC module as provided. See DOI: 10.1039/c3nr02107f

‡ Yu-Ting Liu and Chiun-Yi Wu have equally contributed to this work.

Published on 19 July 2013. Downloaded by Synchrotron Radiation Library on 25/11/2013 06:52:47.

To optimize the activity of CNCs, previous studies have elucidated how the kinetics of the redox reactions is affected by using binary nanoalloy or compounds NPs in DSSC.[3,6] However, the important question that has yet to be confirmed is how to manipulate the atomic structure at the heterogeneous surface of CNCs so the DSSC efficiency can be substantially improved. Core–shell type NPs could be an important platform to study these mysteries due to their superior surface activity, prolonged chemical stability, and simplicity of the surface heteroatomic environment.[16,18,19] On such a platform, our previous studies had shown the capability to control the growth of external shell crystallites along with the surface activity of core–shell CNCs by carefully selecting the core crystallite components and precisely growing the shell thickness.[20–22] In this study, we demonstrate that when the conventional platinized cathode is replaced by Co_3O_4–Pt core–shell cathodic nanocatalysts (denoted as C/P CNCs) with proper composition and atomic structure, the efficiency of DSSC can be substantially improved. As compared to monometallic Pt NPs, these C/P CNCs not only catalysed the I_3^- reduction reaction to a greater degree, thereby boosting the photovoltaic efficiency of DSSC by ~21%, but also reduced the Pt loading by more than ~60%. The insight into the mechanism of the enhanced performance by C/P CNCs was obtained by examining the effects of core–shell interface on the surface structures along with electrochemical properties by using X-ray spectroscopic techniques, electrochemical analyses, and photovoltaic characterizations.

Experiments

Synthesis of Co_3O_4–Pt core–shell CNCs with different shell thicknesses

The synthesis of C/P CNCs was conducted by combining chemical reduction and polyol reaction. In the first step, cobalt core NPs were grown by a wet chemical reduction method. It was conducted by adding 10 ml of 300 mM sodium borohydride [$NaBH_4$] water solution into 40 g of 20 mM cobalt acetate tetrahydrate [$C_4H_6CoO_4 \cdot 4H_2O$] ethylene glycol (EG) solution in the presence of 10 wt% of polyvinylpyrrolidone stabilizer (PVP-40, MW = 40 k). The solution of PVP blended Co NPs (Co–PVP) was re-dispersed in EG into a metal containing 10 mM and then heated to 160 °C to dehydrate for 2 h. After dehydration and cooling to room temperature, the Pt shell crystal was grown by mixing Co–PVP with hexachloroplatinic acid [$H_2PtCl_6 \cdot 6H_2O$] in a Pt/Co ratio of 1 and was then treated at 160 °C for another 2 h. The entire procedure was conducted under ambient atmosphere. The detail procedures and mechanisms for the experimental parameters and the corresponding nucleation growth are given in the ESI† and our previous studies.[20–22] The NPs extracted EG were re-dispersed in ethanol to form slurry. This slurry was spin-coated onto FTO glass followed by annealing at 330 °C for 30 min to produce the cathode (for the DSSC system). The anode contained ~20 μm thick P25 (commercial titanium oxide NPs in an average size of 25 nm) thin film (working area = 25 mm^2) onto an FTO glass. This anode was annealed at 450 °C for 30 min and then immersed into N719 dye solution (20 mg of N719 in 67.5 ml of EtOH) for 24 h. The I/LiI–TPB–MPN electrolyte was prepared by dissolving 0.253 g of I_2 (0.05 M), 1.352 g of LI (0.5 M), and 1.339 g of TBP (1.339 g) in a MPN solvent (20 ml). Detailed procedures for growing the CNCs and assembling the DSSC system are given in the ESI in Fig. S1.†

NCs characterizations

The physical properties of C/P CNCs were characterized by various techniques including small-angle X-ray scattering (SAXS), X-ray absorption spectroscopy (XAS), X-ray diffraction (XRD) at beamlines of BL-23A, BL-17C, and BL-01 at NSRRC (Taiwan), respectively. The high resolution XRD patterns were collected at beamline of BL-12B2 at Spring-8 (Japan). The photovoltaic efficiency of the DSSC was measured under full-sun illumination (AM 1.5 G) by using a standard potentiostat (Keithley 2400 equipped with a solar simulator Newport 3A). The working cathode was prepared by spin coating the slurry of NCs on a commercial available fluorine-doped tin oxide (FTO) glass with a post heat treatment at 330 °C for 30 min under air atmosphere. The details of electrochemical experiments and X-ray characterizations are reported in the previous studies.[20]

Results and discussion

Our previous works had successfully engineered the surface activity and structure stability of core–shell anodic nanocatalysts (ANCs) by controlling the thickness of electrochemically active atom (Pt) onto different type of core crystallites.[20–22] In this study, by applying the engineering approaches, how the C/P CNCs improve the power efficiency of a DSSC system will be systematically elucidated. Compared to Pt NPs, C/P CNCs with near-monolayer thick of Pt shell improves the power efficiency and current density of DMFC by more than ~36% and ~21%, respectively. To clarify the hindered mechanisms, the surface electronic properties of C/P CNCs correlating to the performance of DSSC are investigated. From these results, we elucidate the predominate mechanism (*e.g.*, bifunctional effect, ligand effect, lattice strain, and surface atomic packing)[13,17,23,24] on C/P CNCs that been manipulated to optimize the DSSC efficiency. Hereby, the DSSC with Pt NPs cathode is prepared and the corresponding structure to electrochemical correlations is presented as a reference.

Nanostructure and shell thicknesses determination

The nanostructure of as synthesized electrocatalysts is elucidated by using small-angle X-ray scattering (SAXS) analysis and the experiment spectra [$I(q)$ *vs.* q] of Pt and C/P CNCs that containing different Pt/Co ratios are shown in Fig. 1a. Since the surface catalytic activity is the major concern, only the intra-particle structure information (*i.e.* particle shape, average size, and configuration) which corresponds to the scattering oscillation in the range $q > 0.08$ Å^{-1}, is discussed here. As illustrated, the indistinct scattering hump across the range 0.08 Å^{-1} < q < 0.36 Å^{-1} is due to the edge smearing effect of rectangular-like Pt NPs (as probed by the high resolution transmission electron microscopy HRTEM images in Fig. 3) on the SAXS feature. On the other hand, the spectra of C/P CNCs show the periodic

 This journal is © The Royal Society of Chemistry 2013

Published on 19 July 2013. Downloaded by Synchrotron Radiation Library on 25/11/2013 06:52:47.

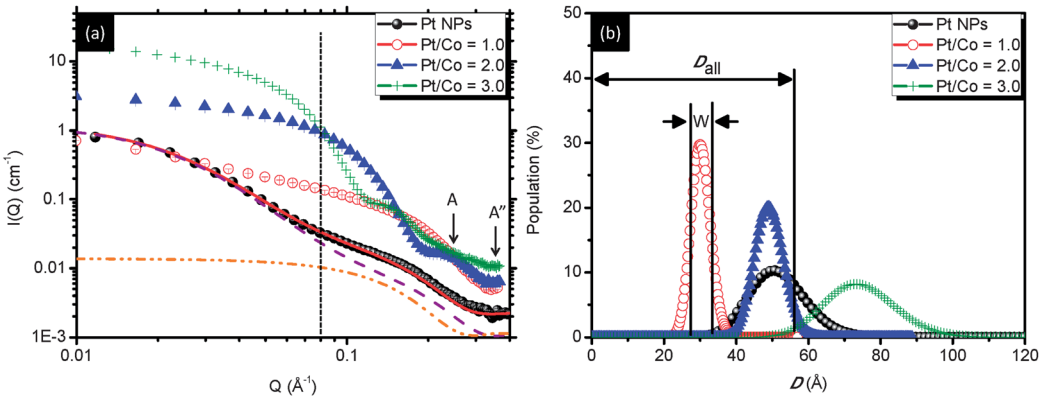

Fig. 1 (a) The small-angle X-ray scattering patterns with fitting curves of Co–Pt core–shell NPs and Pt NPs and (b) the corresponding particle size distribution curves. Only the Pt NPs case is shown and cases for other NPs are given in the ESI in Fig. S2.†

scattering humps (denoted by A and A″) with considerable intensity extending to the q range of up to 0.36 $Å^{-1}$, which typifies the typical SAXS feature of NPs with a core–shell structure.[25,26] The structural parameters for the two types of NPs are obtained by fitting their SAXS spectra with adequate models and the obtained results are summarized in Table 1 (the fitting curves for the experimental spectra are shown in Fig. S2† and the inter-particle structural parameters are given in Table S1†). Accordingly, the Pt NPs possess an average particle size (D_{NPs}) of 4.24 nm and a polydispersity of particle size W/D_{all} = 27.1%. In comparison, the Co_3O_4–Pt core–shell CNCs are grown into spherical particles. Moreover, for the increasing Pt/Co ratio from 1.0 to 3.0, the core diameter (D_C) and shell thicknesses (T_S) are increased from 2.52 to 2.88 nm and from 0.25 nm to 7.66 nm, respectively. The growth of C/P CNCs with core–shell structure is evident since the polydispersity of the particle size is quite small (<15%) as determined from the SAXS analysis in Fig. 1b.[20] In the meantime, the increase of Co core is a clear indication for the Pt to Co replacement upon growing the shell crystal with high content of excess Pt anions in the colloid solution system.

Determination of core crystallites and lattice strain in shell region of core–shell NCs

After revealing the formation of heterogeneous junction at core–shell interface of C/P CNCs by SAXS, we can consider that the lattice strain within Pt shell crystal is mainly dominated by the lattice structure differences between core and shell crystallites. The crystal structure of core and shell regions was determined by XRD to clarify how the surface lattice strain is manipulated by varying the shell crystal thickness. Before the XRD measurements, the CNCs were dispersed at the surface of the silicon wafer and were treated by the same thermal conditions with which they are treated for CV analysis. Fig. 2 compares the XRD patterns of Pt NPs (Fig. 2a), and C/P CNCs of Pt/Co ratios = 1.0 (Fig. 2b), 2.0 (Fig. 2c), and 3.0 (Fig. 2d), respectively. The corresponding structure parameters are summarized in Table 2.

As demonstrated in Fig. 2a, the two diffraction peaks at 28.79° (A) and 33.76° (B) correspond to the metallic characters from (111) and (200) facets of Pt NPs with an average coherent length (D_{avg_Pt}) of 5.45 and 4.67 nm, respectively, according to the Debye–Scherrer equation. The C/P CNCs is a two-phase coexisting system. For C/P CNCs of Pt/Co = 1.0 (see Fig. 2b), the diffraction peaks D and E correspond to the characteristic signals from the (311) and (222) facets of Co_3O_4 phase with a D_{avg} of 5.05 nm and 1.17 nm, respectively. The peaks F and G could be attributed to the diffraction signals from cobalt carbide complex (CoC_2, S. J. Nagakura, *et al.*, *J. Phys. Soc. Jpn.*, 1961, **16**, 1213) with a D_{avg} of 2.35 nm (at (020) facet) and 37.29 nm (at (210) facet), respectively. These giant carbide NPs might originated from the sintering of polymer blended Co NPs and Co precursor (*i.e.*, Co–acac or Co–pyridine complexes) retentions during the preparation of XRD samples. The broad peaks of A and B denote the formation of Pt fcc (111) and (200) facets with an estimated D_{avg_Pt} of 1.89 to 1.16 nm. By increasing the Pt/Co ratio to 2.0, the D_{avg_Pt} at (111) and (200) facets increase to 3.98 nm and 2.11 nm, respectively. Such uneven crystal growth suggests the preferential ligand stabilization at opened surface (*i.e.*, (200) facet). Further increasing Pt/Co to 3.0 results in the growth of Pt crystallite to ~5.29 nm (at (111) facet), the formation of $Co_2(CO)_8$ crystallite (denoted by peak C, ICSD #72-1086) with a size of 91.23 nm, and the suppression of CoC_2 crystallite (*i.e.*, dissolving the retained polymer blended Co NPs). Both the three indications are direct evidence of the substantial Pt cation to Co atom transmetalation. This hypothesis is further explained by the changes of Co_3O_4 coherent length at (311) and

Table 1 SAXS determined structure parameters of Pt NPs and Co–Pt core–shell NCs

NPs[a]	D_C (nm)	T_S (nm)	D_{NPs} (nm)	W/D_{all} (%)
Pt NPs	NA	NA	4.24	27.1
Pt/Co = 1.0	2.52	0.25	3.02	8.9
Pt/Co = 2.0	2.89	0.98	4.85	9.1
Pt/Co = 3.0	2.88	2.39	7.66	15.0

[a] D_C: core dimension, T_S: shell thickness, D_{NPs}: particle dimension, W/D_{all}: polydispersity of particle size.

Published on 19 July 2013. Downloaded by Synchrotron Radiation Library on 25/11/2013 06:52:47.

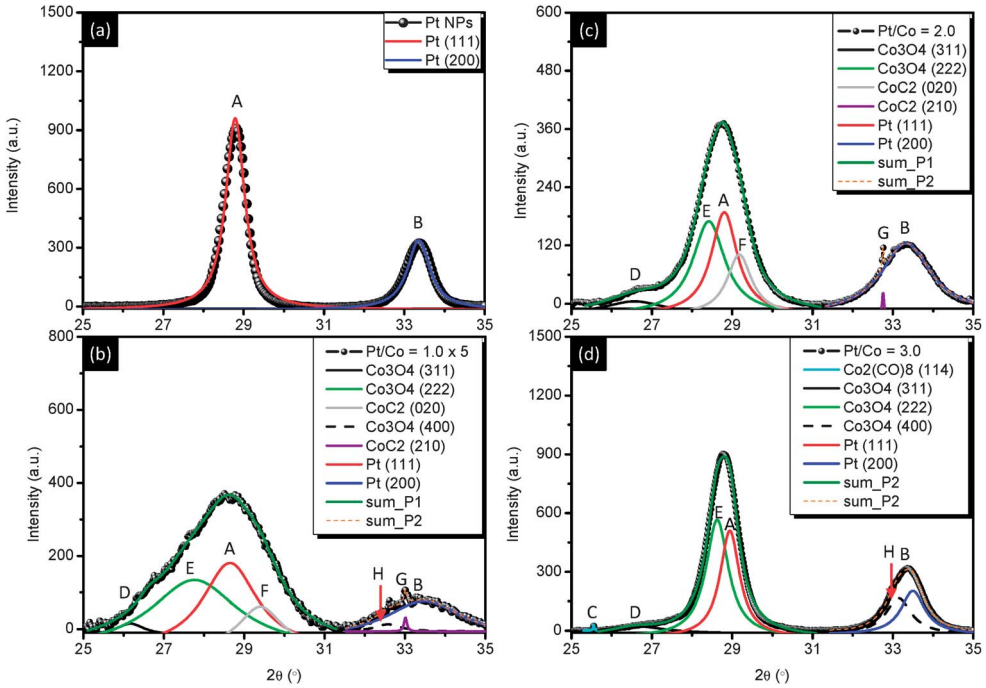

Fig. 2 XRD patterns of Pt NPs and Co–Pt core–shell NCs.

(222) facets with the Pt/Co ratio. During which, as shown in Table 2, the D_{avg} at (311) and (222) facets of Co_3O_4 are found changing in different trends; the former decreases from 5.05 to 1.76 nm and the later increases from 1.17 to 4.61 nm, respectively, revealing the preferential restructure of Co atom to the close packed facets by Pt-to-Co transmetalation simultaneously with the stabilization of Co_3O_4 crystallite at the opened facets by the pyridine ligands. Such transmetalation *via* Pt complex (Pt^{4+}–P) is triggered by the substantial electronegativity difference between Pt and Co atoms.[27,28] It forms the Pt clusters at Co_3O_4 surface (Pt^C@Co_3O_4–acac) and leads to the dissolution of Co cations. The Co cations will be chelated by pyridine ligands in a form of Co^{2+}–P^{ex} (see eqn (1)):

$$Co_3O_4\text{–acac} + Pt^{4+}\text{–P} + Co\text{–acac}^R \rightarrow Pt^C@Co_3O_4\text{–acac} + 2Co^{2+}\text{–}P^{ex} + Pt^{4+}\text{–}P^R \quad (1)$$

Table 2 XRD determined structure parameters of Pt NPs and Co–Pt core–shell NCs

NPs	Peak	Index	2θ (°)	$\Delta 2\theta$ (°)	D (nm)	d (Å)	a (Å)
Pt NPs	A	Pt (111)	28.79	0.57	5.45	2.26	3.921
	B	Pt (200)	33.36	0.68	4.67	1.96	
Pt/Co = 1.0	A	Co_3O_4 (311)	26.63	0.61	5.05	2.44	
		Co_3O_4 (222)	27.76	2.65	1.17	2.35	
		Pt (111)	28.64	1.65	1.89	2.28	3.941
		CoC_2 (020)	29.39	1.33	2.35	2.22	
	B	Co_3O_4 (400)	32.58	0.75	4.19	2.01	
		CoC_2 (210)	33.01	0.08	37.29	1.98	
		Pt (200)	33.48	2.33	1.36	1.95	
Pt/Co = 2.0	A	Co_3O_4 (311)	26.57	1.88	1.65	2.45	
		Co_3O_4 (222)	28.42	0.97	3.22	2.29	
		Pt (111)	28.8	0.78	3.98	2.26	3.925
		CoC_2 (020)	29.17	0.75	4.18	2.24	
	B	CoC_2 (210)	32.75	0.05	62.01	1.99	
		Pt (200)	33.32	1.50	2.11	1.96	
Pt/Co = 3.0	D	$Co_2(CO)_8$ (114)	25.55	0.03	91.23	2.55	
	C	Co_3O_4 (311)	26.57	1.77	1.76	2.45	
	A	Co_3O_4 (222)	28.62	0.68	4.61	2.28	
		Pt (111)	28.84	0.59	5.29	2.26	3.922
	B	Co_3O_4 (400)	33.14	0.76	4.12	1.97	
		Pt (200)	33.41	0.71	4.42	1.96	

This journal is © The Royal Society of Chemistry 2013

Published on 19 July 2013. Downloaded by Synchrotron Radiation Library on 25/11/2013 06:52:47.

The retained Pt (Pt^{4+}–P^R) and excessed Co (Co^{2+}–P^{ex}) complexes will interact with the CHO: radicals to form the shell crystals on the Co_3O_4 core ($Pt^S_{1-x}Co_x$@Co_3O_4–P) in polyol reaction (eqn (2)):

$$Pt^C@Co_3O_4\text{–acac} + 2Co^{2+}\text{–}P^{ex} + Pt^{4+}\text{–}P^R + CHO: \rightarrow Pt^S_{1-x}Co_x@Co_3O_4\text{–}P + Co^{2+}\text{–}P^R \quad (2)$$

By interacting with the CHO: radicals and the subsequent thermal anneal (during oxidation) the retained Co-complexes (Co^{2+}–P^{ex}) would transform to the Co carbon crystallite (Co–C^C, *i.e.*, CoC_2 and $Co_2(CO)_8$) (eqn (3)):

$$Co^{2+} - P^{ex} + CHO: \xrightarrow{\Delta} Co - C^C \quad (3)$$

The phase transformation of cobalt in the C/P CNCs (eqn (1) and (2)) and the metallic complex (eqn (3)) are further illustrated by XAS analysis in the ESI (see Figure S3, S4, and Table S3†). Accordingly, the coordination numbers of Co–C and Co–O bond pairs are found changes in opposite trends by increasing Pt/Co ratios. It shows the consistent results with XRD analysis which suggesting that part of Co atoms on C/P CNCs will transform to Co complex by Pt cations. For the case of Pt/Co = 2.0, these Co complexes will interact with the CHO: radicals and then form the $Pt_{1-x}Co_x$ surface alloy at the CNCs. By increasing Pt/Co to 3.0, substantial amount of the Co atoms will be deported from C/P CNCs by transmetalation pathway and form the Co-complex. In this case, the Co-complexes will process two pathways to form crystalline structure including the formation of $Pt_{1-x}Co_x$ surface alloy at the CNCs and the nucleation and growth of Co carbide crystalline. The former is triggered by the simultaneous Pt and Co reduction by CHO: during the polyol reduction and the latter is by the thermal reduction of retained Co cations by pyridine and embedded CHO: in the polymer stabilizers during the subsequent annealing processes. During the polyol reduction, the subsequent Pt shell growth will embed the Co atoms due to the high ratio of Pt/Co and then suppress them from bonding with the oxygen atoms in ligands (*i.e.*, pyridine and acac). On the other hand the retained Co will form cobalt carbide crystalline as consistently shown by the crystal growth of Co–C^C in XRD analysis.

The XRD results also reveal the lattice strain of C/P CNCs. As shown in Table 2, the Pt shell crystallites experience a lattice expansion that decreases from ~0.51% to ~0.02% with increasing Pt/Co ratios from 1.0 to 3.0. This lattice relaxation finely obeys the results of theoretical DFT prediction and experiment on the thin-film and core–shell NPs systems upon growing the capping film on a single crystal (core crystal) surface with increasing thickness.[17,20,22] In addition, as indicated by the growth of core dimension by SAXS (Table 1), the heteroatomic intermix between core–shell components is unavoidable due to the spontaneous replacement of Co atoms by Pt cations followed by the polyol reduction of the retained metallic complexes (Co and Pt) in the reagents.[28] Consequently, this heteroatomic intermix will induce a certain extent of surface alloying that modifying the surface reactivity of C/P CNCs.

Effects of shell crystallite thicknesses on the lattice structure of core–shell NCs

The lattice structures of the three C/P CNCs (with identical annealing treatment to that of XRD and the subsequent electrochemical and photovoltaic analyses) are elucidated by using HRTEM (Fig. 3 and Table 3). As shown in Fig. 3a, the interplanar spacing of the Pt NPs is estimated to be 1.98 ± 0.01 Å corresponding to that of Pt fcc (200). A severe interparticle sintering is found in Pt NPs (see the insets), driven by a lowering of Gibb's free energy due to a reduction of surface area. Fig. 3b shows the HRTEM images for the Pt/Co = 1.0 CNCs. As indicated, the Pt/Co = 1.0 CNCs grows in isomeric symmetry without preferential facets. Such uniform shell thickness is expected because the Co core crystal is well protected by capping polymers into a spherical particle without exposing specific facet to the reactants prior to the Pt shell deposition. It possesses an average size of 3.5 nm and a rough surface. The interplanar spacing across the arrow direction is determined to be 2.39 ± 0.01 Å corresponding to that of Co_3O_4 {222} (JCPDS #65-3103) and Pt {111} facets (JCPDS #88-2343) and the lattice constant of 4.14 ± 0.01 Å. This lattice constant is ~4.5% larger than that of fcc Pt NPs (3.96Å ± 0.01 Å), therefore suggesting the lattice expansion in Pt region of Pt/Co = 1.0 CNCs. The HRTEM image of Pt/Co = 2.0 CNCs is shown in Fig. 3c. It depicts the formation of high roughness surface since the shell crystal are built by growing Pt atoms at Co_3O_4 core crystallite surface through the spontaneous transmetalation reaction basing on the heterogeneous nucleation–growth model with the consideration of geometry effects on evaporation–condensation pathways at core NPs.[29] Fig. 3d shows the HRTEM image of Pt/Co = 3.0 CNCs. It clearly depicts

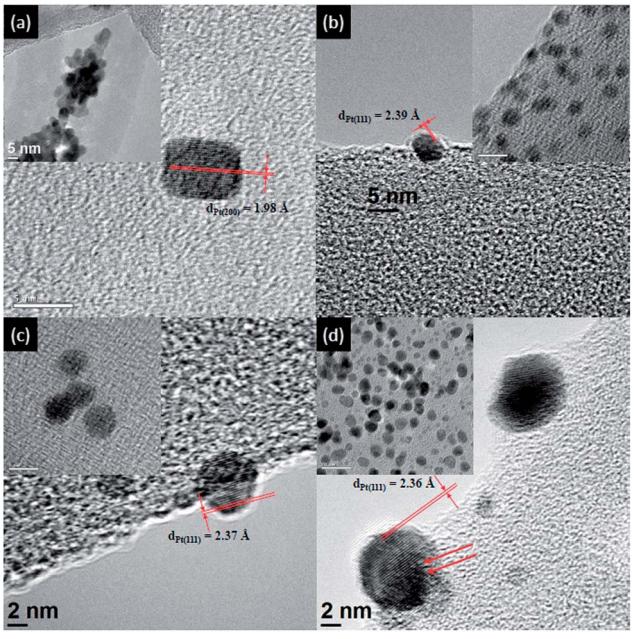

Fig. 3 High resolution transmission electron microscopy (HRTEM) images of Co–Pt core–shell NPs with the Co/Pt ratios of (a) 1.0, (b) 2.0, (c) 3.0, and (d) Pt NPs; insets demonstrated the TEM images of corresponding NPs annealed at 330 °C for 30 min.

Published on 19 July 2013. Downloaded by Synchrotron Radiation Library on 25/11/2013 06:52:47.

Table 3 HRTEM determined structure parameters of Co–Pt core–shell NPs and Pt NPs

NPs	Index	d (Å)	a (Å)	ε^a (%)
Pt NPs	Pt {200}	1.98	3.96	NA
Pt/Co = 1.0	Co_3O_4 {222}/Pt {111}	2.39	4.14	−4.5
Pt/Co = 2.0		2.37	4.10	−3.6
Pt/Co = 3.0		2.36	4.08	−3.2

[a] ε: lattice strain.

the inner particle interface (denoted by the arrows) again probing the growth of core–shell NPs. From HRTEM image we can notice that the Pt/Co = 3.0 CNCs grows into Pt fcc phase. The lattice fringes of these particles are found to have an average inter-planar spacing of 2.36 Å ± 0.01 Å, which is in agreement with that of Pt fcc (111) facet. Meanwhile, it is important to note that the lattice expansion was progressively reduced from −4.5% to −3.2% which indicating that the surface heterogeneous activity of the core–shell CNCs can be manipulated by controlling the shell crystal thicknesses.[16,20] In addition, a certain extent of inter-particle sintering is found between the C/P CNCs. This sintering is attributed to the interparticle Pt atom rearrangements upon preparing the CNCs cathodes during annealing.[14,20]

Effects of shell thicknesses on atomic structure and local electronic structure of shell crystal in core–shell NCs

Combining the effects of lattice expansion with heteroatomic intermix,[23] the local atomic and electronic structures of Pt atoms could be modified (*i.e.*, the ligand effects and bifunctional mechanisms) and thus the redox activity of core–shell NPs is improved.[16,18,21,30] From previous DFT calculations and experiment results, the lattice strain is the main driving force for the heteroatomic interaction between Co and Pt atoms in core–shell CNCs.[16,18] The lattice expansion enables the charge injection from Co to Pt atoms therefore facilitates the capabilities of core–shell CNCs for I_3^- to I^- reduction. Fig. 4 shows the Pt XANES spectra of Pt NPs and C/P CNCs of different Pt/Co ratios, respectively. In Fig. 4a, the intensity of the L_3-edge white-line H(L_3) reflects to the occupancy of the 5d orbital.[31] Based on this concept, it is expected to note that the H(L_3) value would increase with decreasing 5d orbital occupancy of Pt atoms. Therefore, the fact of observing the largest H(L_3) of Pt/Co = 1.0 NPs indicating its highest extent of Pt heteroatomic interaction (*i.e.*, oxygen in platinum oxide or chemisorption oxygen at metallic Pt) among experiment catalysts. Hence, the decreasing H(L_3) of CNCs is understandable due to the decreasing heteroatomic conjunction of Pt to surface oxygen atoms and core Co atoms by increasing the Pt/Co ratio from 1.0 to 3.0.

The heteroatomic electronic interaction at the core–shell interface of C/P CNCs (including the oxidation of Pt and oxygen chemisorption at Pt and the conjunction between Pt, oxygen, and Co_3O_4 core atoms) can be further clarified by the Pt L_2-edge XANES in Fig. 4b. As indicated, the strongest H(L_2) suggests that the highest extent of inner sphere Pt–O chemisorption of Pt NPs

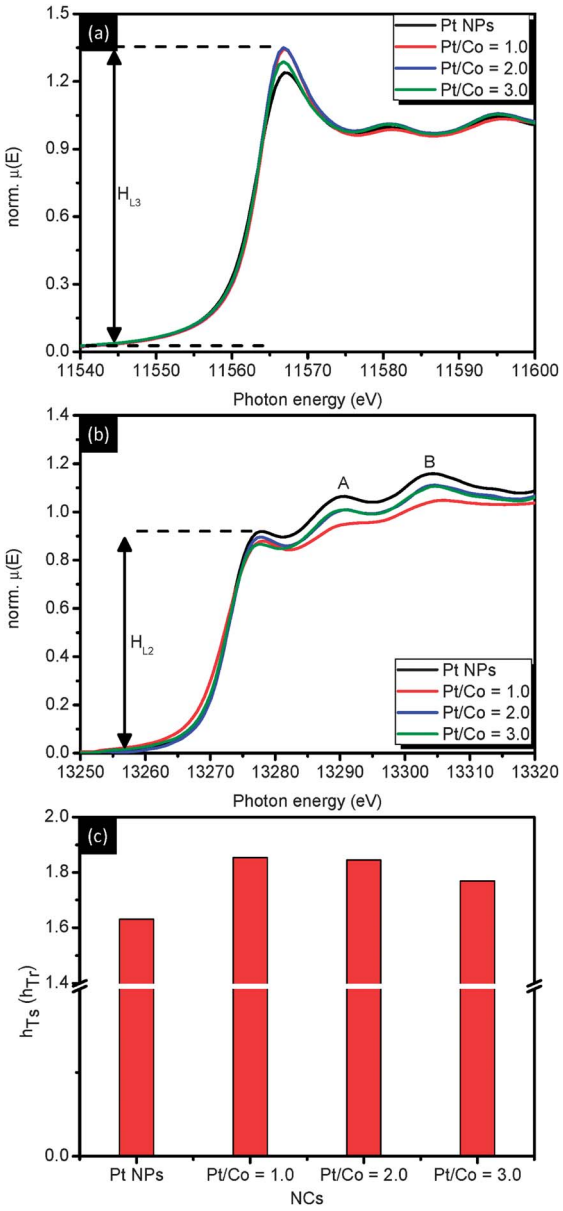

Fig. 4 The X-ray absorption near-edge structure spectra of Co–Pt core–shell NPs and Pt NPs at (a) Pt L_3- and (b) Pt L_2-edges. (c) The estimated Pt 5d orbital unfilled density of state of experiment CNCs.

(*i.e.*, oxygen chemisorption) among all CNCs. This is because the Pt atoms exhibit a strong tendency to restructure themselves into clusters to reduce the excess surface free energy[14,26] (revealed by the strong post-edge multiple-scattering oscillations at A and B peaks and the large Pt–Pt coordination number in Table S2 and Fig. S3†) instead of forming the platinum oxide (or compound). For C/P CNCs, the weaker post-edge oscillations indicate their lower extent of Pt homoatomic interactions compared to that of Pt NPs. Consequently, the weakest post-edge oscillations refers to the lowest Pt homoatomic interactions of Pt/Co = 1.0 among all CNCs. In C/P CNCs, majority of Pt atoms are subjected to the heterogeneous interface. These interfacial Pt would interact with neighbouring atoms (oxygen

 This journal is © The Royal Society of Chemistry 2013

Published on 19 July 2013. Downloaded by Synchrotron Radiation Library on 25/11/2013 06:52:47.

in Pt–O, Co_3O_4, Pt oxide, and Co in Co_3O_4 core), and thus forming the complex ternary Pt–Co–O electronic interactions.

The Pt h_{Ts} value provides direct evidence to the lattice strain effect on the heteroatomic electronic interaction of Pt and C/P CNCs. Fig. 4c illustrates the corresponding h_{Ts} of the experiment CNCs that quantified by a well-known L-edges correlation developed by Mansour *et al.*[31,32] The h_{Ts} is dominated by structure factors such as morphology, particle size, heteroatomic intermix, and the extent of oxidations of the NPs.[33] Accordingly, the h_{Ts} of Pt NPs is found 1.63-fold to that of Pt foil. Given that the heteroatomic intermix is absence, the higher h_{Ts} of Pt NPs than Pt foil can be attributed to mainly the particle size effect and partially a certain extent of the surface oxidization and oxygen chemisorption. On the other hand, for C/P CNCs, the h_{Ts} could be the consequence of the competition between Pt–Co and Pt–O heteroatomic hybridizations in the presence of lattice strain and domain size effects. In this case, the Pt–Co bond induces a substantial extent of valence charge injection from Co to Pt atoms and the Pt–O withdraws a considerable valence charge from Pt to O. Taking all valence charge transition pathways together, the slightly increased h_{Ts} is possibly due to its lower homoatomic coordination number of Pt domain (see Fig. S3 and Table S2†) and the stronger extent of surface oxidation (or oxygen chemisorption) and heterogeneous interface contact than Pt NPs.[18,20]

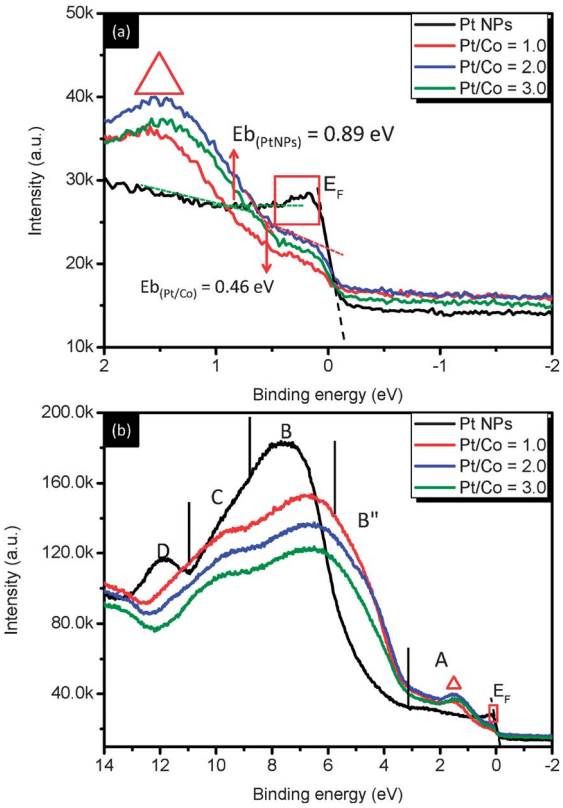

Fig. 5 The valence band spectra of the Pt NPs compared with that of Co–Pt core–shell NPs in different Pt/Co ratios (a) enlarged region A and (b) full spectrum.

Effects of shell thicknesses on valence band structure and surface binding energy (E_b) of core–shell CNCs

The proposed charge transfer from Co to Pt induced by lattice strain and the Pt E_b shift of C/P CNCs are further supported by the valence band photoemission (VB) spectra (enlarged region A in Fig. 5a and full spectrum in Fig. 5b). As can be seen, the VB spectrum of the Pt NPs is consisted of several features: a steep increase in the binding energy range of 0–0.24 eV, the flat stage with a reflection point (*i.e.*, E_b) at 0.89 eV, a shoulder till 3.08 eV (region A), and three additional broad-bands centred at 7.57 eV (region B), 10.02 eV (region C), and 11.95 eV (region D). These distinguished features correspond to that of bulk Pt samples with ordered crystal facets and resembled the metallic Pt 5d-states of Pt NPs.[34] Compared to Pt NPs, the C/P CNCs lower the surface E_b by 0.43 eV (at 0.46 eV). It forms a shoulder (B′′) across A–B bands, broadens the VB, and shifts down the sub-level bands (C and D) by 0.86 eV. Since its intensity of VB spectrum below Fermi level is normalized to be the same, the slight decrease of outmost band intensity (denoted by an open rectangular in region A) could be attributed to the valence charge relocation from Pt to oxygen (in surface platinum oxide and oxygen chemisorption). It indicates a slight decrease of density of states (DOS) as that consistently revealed by their higher h_{Ts} than Pt NPs (see Fig. 4c). In addition, the higher VB intensity below the E_b level (in A and B′′ regions) is observed. It is the direct evidence for the abundant valence charge transition from Co to Pt and can be explained by the low electronegativity of Co and the lattice expansion in Pt shell as consistently been predicted by the DFT simulations[16–18] and the above XAS characterizations.

The VB photoemission spectrum of C/P CNCs with uncompleted Pt shell (Pt/Co = 0.5) is compared as a reference in Fig. S5.† As can be seen, the Fermi level (E_F) of Pt/Co = 0.5 NPs was increased by 1.8 eV compared to the Pt NPs. In the meantime, its sub-level VBs (in region B and C) were split into 3 bands (2, 3, and 4) which is possibly due to the strong charge donation to the near-surface Pt atoms and the localization of retained valence electrons in Co core atoms by the lattice strain. Such distinct band features clearly reveal that the obtained spectra of experiment CNCs (Pt NPs and C/P CNCs with Pt/Co > 1.0) could not be thought of as the sum of separate cobalt and platinum contributions. Instead, it resembles the effects of sub-layer core crystal (the Co_3O_4 core crystallite) on VB structures of outer layer Pt atoms. Hereby, the substantial increasing of outer band (region A and B′′) intensity is the feature indicating that the considerable amount of valence charge injection from Co to Pt and the localization of these electrons in the sub-core level region due to the strain induced interfacial Pt–Co coupling. This coupling rationalizes the decrease of E_b. Meanwhile, the down-shift of sub-level bands and the slight increase of DOS imply the trend of valence charge relocation at the top most layer Pt atoms. These features are consistent with the DFT predictions in the literatures which suggesting that easy chemisorption of anions on the Co–Pt surface sites and the charge translocation to the adsorbed anions from the VB of CNCs. With such properties, the C/P CNCs could reduce the potential barriers for I_3^- to I^- reduction to improve the DSSC performances.[20,23,35]

Published on 19 July 2013. Downloaded by Synchrotron Radiation Library on 25/11/2013 06:52:47.

Photovoltaic performance of core–shell CNCs

Having disclosed the structural properties of C/P CNCs *via* spectroscopy analyses; here we demonstrate their electrochemical performances, particularly, in the I_3^- reduction activity at a cathode which substantially influences the photovoltaic performance of DSSC The activities of NPs over I_3^- reduction were determined by cyclic voltammetry (CV) using a three-electrode system set-up, in which the fluorine-doped tin oxide (FTO) working electrode (a sheet resistance of 12 Ω sq^{-1}) was spin coated with the four types of CNCs as catalyst. Fig. 6a presents the CV spectra of the four catalysts measured at a potential scan rate of 30 mV s^{-1} with a step of 5 mV, where four current maximum peaks corresponding to their reactions with I_3^-/I^- couples are indicated by the arrows with capital letters. As indicated that the forward potential sweep of C/P CNCs shifts to more oxidative potentials relative to peak A (347.0 mV) and B (778.7 mV) of Pt NPs by ~10 mV by growing the Pt/Co = 1.0. Further increasing the Pt/Co ratio (till 3.0) restores the metallic Pt characters of the C/P CNCs, and thus shifts the I^- (A) and I_3^- oxidation peaks (B) back to the normal positions of Pt NPs. Likewise, the reverse potential scan of C/P CNCs also shifts to more oxidative potentials with a considerable shift (34.1 mV) of peak D from $V_D^{Pt} = 34.0$ mV to $V_D^{C/P} = 68.1$ mV. Kinetically, these shifts refer to the fact that oxidations of I^- ($3I^- \rightarrow I_3^- + 2e^-$, A) and I_3^- ($2I_3^- \rightarrow I_2 + 2e^-$) and reduction of I_2 ($3I_2 + 2e^- \rightarrow 2I_3^-$, peak C) and I_3^- ($I_3^- + 2e^- \rightarrow 3I^-$, D) are all slightly faster when catalysed by C/P CNCs than by their Pt counterparts. In brief, if the kinetics of redox reactions is faster, the reaction equilibrium can be established more rapidly to convert more reactants. Consequently, the current density takes shorter time to respond to the applied voltage, thus it ramps up quicker (*i.e.*, lower charge transfer resistance) and peaks at an earlier reductive potential.[36] For the case of Pt NPs, the maximum current density of the I_3^- reduction ($J_D^{Pt} = 0.77$ mA cm^{-2}) is 45.3% smaller than that of I^- oxidation ($J_A^{Pt} = 1.41$ mA cm^{-2}) implying that a significant passivation of the catalyst surface by the I_2 chemisorptions.[36] On the other hand by using C/P CNCs, the maximum current densities ($J_D^{C/P} = 1.06$ mA cm^{-2} and $J_A^{C/P} = 1.71$ mA cm^{-2}) are both enhanced by35.9 and 21.2% by the optimized ratio of Pt/Co = 1.0, respectively. Particularly, the enhancement of the Pt surface activity by the Co core over I_3^- reduction is of critical importance for the photovoltaic efficiency of DSSCs since this reaction is known to possess a prohibitively slow kinetics.[36]

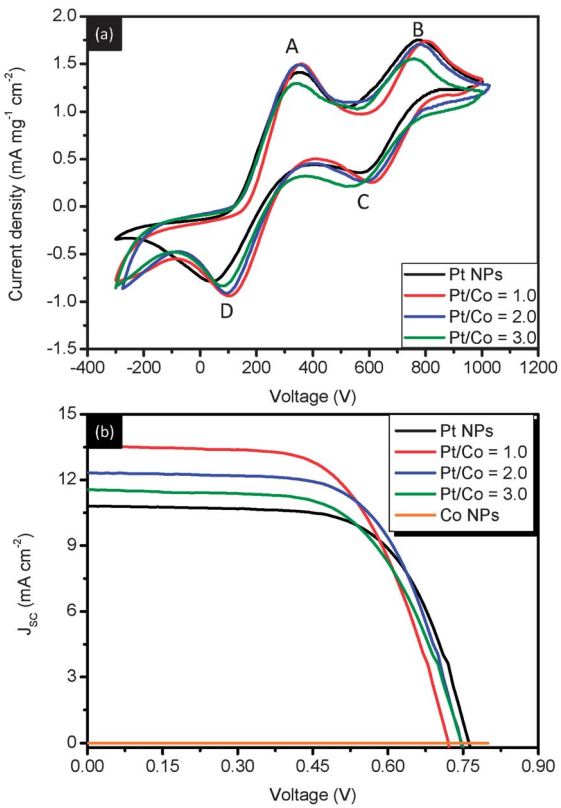

Fig. 6 *J–V* (a) and *C–V* (b) characteristic curves of the Pt NPs and C/P CNCs of different Pt/Co ratios. The electrolyte is acetonitrile solution consisted 10.0 mM of LiI and 1.0 mM of I_2. These data were measured at a potential sweeping rate of 30 mV s^{-1}.

The improved I_3^- reduction activity of C/P CNCs on promoting the DSSC is directly illustrated by the photovoltaic (PV) measurement (see the current density–voltage (*J–V*) curves in Fig. 6b with the photovoltaic parameters given in Table 4). Accordingly, compared to Pt NPs, the C/P CNCs cathode with the value of Pt/Co = 1.0 increases the short-circuit density current, J_{SC}, by 22.9% (from 11.01 to 13.53 mA cm^{-2}) and decreases slightly the open-circuit voltage, V_{OC}, by 0.04 V. Consequently, such cathode enhanced the energy conversion efficiency, $\eta = (FF \times J_{SC} \times V_{OC})/P_{in}$, by ~36.2% (from 4.41 to 6.01%), where FF is the fill factor (see eqn (4)), P_{max} is the maximum electric output power density corresponding to J_{max} and V_{max} indicated in Fig. 6, and $P_{in} = 100$ mW cm^{-2} is the incident light power density.

$$FF = \frac{P_{max}}{J_{SC} \times V_{OC}} = \frac{J_{max} \times V_{max}}{J_{SC} \times V_{OC}} \quad (4)$$

The device performances could be rationalized by the structure parameters including the charge transportation at cathode and the non-radioactive recombination of electrons from TiO_2 NPs to the I_3^- species in the DSSC. Since all the DSSC devices are assembled by identical anode (with the same parameters of porosity, thickness, and working area), the differences of DSSC PV performances could be attributed to the changes of structural parameters of the applied CNCs. These parameters will modify the VB feature (*i.e.*, surface chemical environments) of CNCs and thus dominating the PV characters

Table 4 Photovoltaic performance of full DSSC with cathodes topped with Pt NPs and C/P CNCs

CNCs	η^a (%)	J_{SC} (mA cm^{-2})	FF	V_{OC} (V)
Pt NPs	4.41 ± 0.2	11.01 ± 0.3	0.52 ± 0.02	0.76 ± 0.03
Pt/Co = 1.0	6.01 ± 0.2	13.53 ± 0.2	0.62 ± 0.03	0.72 ± 0.02
Pt/Co = 2.0	5.92 ± 0.3	12.32 ± 0.3	0.64 ± 0.02	0.75 ± 0.01
Pt/Co = 3.0	5.35 ± 0.2	11.56 ± 0.3	0.62 ± 0.02	0.75 ± 0.02

[a] η: photovoltaic efficiency, FF: fill factor, V_{OC}: open circuit voltage.

This journal is © The Royal Society of Chemistry 2013

Published on 19 July 2013. Downloaded by Synchrotron Radiation Library on 25/11/2013 06:52:47.

of DSSC. Our structure characterizations (XAS, SAXS, XRD, and VB) indicating that the Pt shell atoms would receive the valence charge from cobalt oxide (core) and extracting part of these electrons to the surface oxide and oxygen chemisorption. This is the reason that the surface Pt atoms of the C/P CNCs process the similar extent of h_{Ts} (see Fig. 4c) upon varying the Pt/Co ratios. In addition, the ternary Co–Pt–O electronic interactions would generate a slightly opened outmost valence state and a slightly compacted electron field in the sub-level VB region on Pt shell atoms (denoted by an open triangle in the region A, see Fig. 5a). The opened states would facilitate the I^-/I_3^- chemisorption and the compacted electron field would inject the valence charge to assist the reduction of I_3^- into I^- at the CNCs surface. Both the two pathways improve the photovoltaic efficiency of DSSC system. By increasing Pt/Co > 1.0, the sub-level state of core–shell NPs is substantially attenuated due to the reduced valence orbital interaction between Pt and Co atoms. It decreases the J_{SC} of DSSC due to the tardy I_3^- to $3I^-$ reduction at higher DOS, the lower valence charge dissociative (reduced sub-level VB intensity in region B), and possibly the higher d-band centre of core–shell NPs surface compared to that of core–shell NPs with Pt/Co = 1.0. Therefore, in such a way it decreases the DSSC V_{OC} by 0.04 Volt. A crucial point should be noticed is that the faster I_3^- reduction at the C/P CNCs, as compared to Pt NPs, not only the increase of J_{SC} but also the reverse saturation current (J_0) due to the charge recombination of anions at the cathode. Both the increases of J_{SC} and J_0 are due to the rapid I_3^- to $3I^-$ reduction at the low DOS and high valence charge dissociation core–shell NPs surface. In such a way, the high ratio of J_{SC}/J_0 results in the reduction of V_{OC} as discussed above, assuming that $V_{OC} \fallingdotseq (\gamma k_B T/q)\ \ln(1 + J_{SC}/J_0)$ when the anodic I^- digestion rate is relatively slower than that of cathodic I^- production in such a DSSC module.

The above structural parameters complementary with the PV characterizations explain the mechanisms of C/P CNCs (see Fig. 7, the reaction steps are summarized in Table 5) that enhancing the DSSC performance. As clearly indicated by Fig. 4, since the Co atom do not directly participate in the I_3^- reduction (*i.e.*, J_{SC} of DSSC with Co NPs is zero, see Fig. 6), the bifunctional mechanism by surface Co–Pt couples could be ruled out even the surface segregation at C/P CNCs is inevitable. Therefore, the heteroatomic electronic interaction (ligand effect) and the lattice strain of C/P CNCs should play the main role in the PV performance of DSSC. The former is triggered by the larger electronegativity of Pt than Co and the latter is induced by the expansive lattice strain in Pt shell crystal by accommodating at the larger lattice crystallite surface (Co_3O_4 core). Both the two factors induce the charge injection from Co_3O_4 core to Pt shell atoms. They facilitate the I_3^- to I^- reduction and thus improve the DSSC device performance.

The electrochemical impedance spectra which describing the internal resistances and the electron transport kinetics of the DSSC equipped with different CNCs are compared in Fig. 8a (the Nyquist plots with the equivalent circuit in the inset), Fig. 8b (Bode phase plot), and the corresponding electrochemical parameters are summarized in Table 6. These results illustrate the interfacial charge transportation kinetics and thus probing the mechanistic pathways on the improvement of DSSC efficiencies by adopting CNCs with different structure conformations. In general, the three semicircles correspond to the impedances originated from the electrochemical reaction at the CNCs counter electrode (R_2), the charge transfer at the TiO_2/dye/electrolyte (R_3), and the Warburg diffusion process of I^-/I_3^- in the electrolyte (R_4), respectively. In our case, compared to the DSSC with Pt NPs, the charge transport resistance at the cathode/electrolyte (R_2) slightly decreased by 2.4% (from 13.09 Ω to 12.78 Ω) as the cathode was coated by the C/P CNCs of Pt/Co ratio = 1.0. This implies the enhanced interfacial charge transfer kinetics between the Pt sites and I_3^- chemisorptions as a result of the significant charge injection from Co to Pt atoms. This is because the smaller electronegativity of Co than Pt and the lattice expansion within the Pt shell region.

Further increasing the Pt/Co ratios to 2.0 and 3.0 substantially raises the R_2 by 40.5 (18.04 Ω) and 46.3% (19.16 Ω), respectively. Such characters are understandable by considering the lattice relaxation and the substantial increasing of charge acceptor (Pt atoms) to donor ratios (*i.e.*, Pt/Co). The former weakens the lattice field potential between Pt and Co regions, and thus suppresses the Co to Pt charge donation. The later

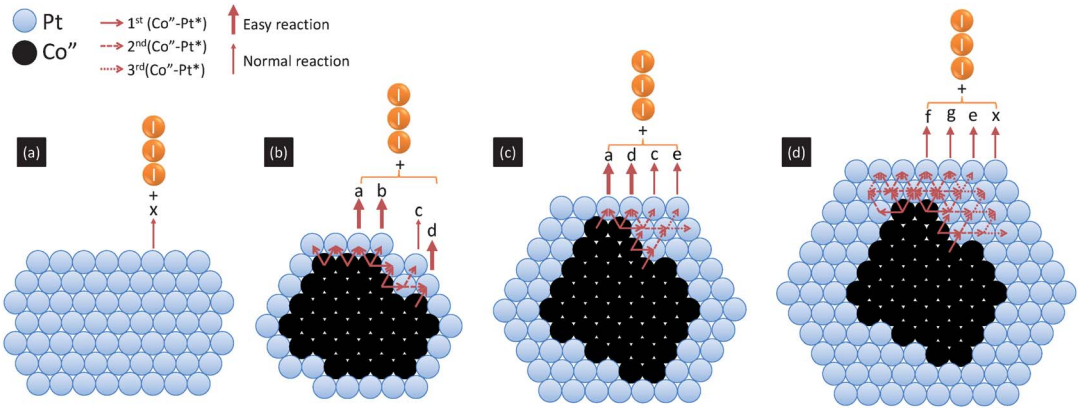

Fig. 7 Proposed schematic representation of the proposed reaction mechanisms for $I_3^- \rightarrow I^-$ redox reaction at (a) Pt NPs, (b) Pt/Co = 1.0, (c) Pt/Co = 2.0, and (d) Pt/Co = 3.0 CNCs, respectively.

Published on 19 July 2013. Downloaded by Synchrotron Radiation Library on 25/11/2013 06:52:47.

Table 5 Proposed reaction mechanisms for I_3^- to I^- redox reaction at experiment CNCs

CNCs	Redox pathway	Reaction site[a,b]
Pt	$I_3^- + (x) = 3I^-$	x: Pt*
Pt/Co = 1.0	$I_3^- + (a, b, c, d) = 3I^-$	a: 2x 1^{st}(Co″–Pt*)
Pt/Co = 2.0	$I_3^- + (e, f, g, h) = 3I^-$	b: 1x 1^{st}(Co″–Pt*)
Pt/Co = 3.0	$I_3^- + (f, g, x) = 3I^-$	c: 1x 2^{nd}(Co″–Pt*)
		d: 1x 1^{st}(Co″–Pt*) + 1 × 2^{nd}(Co″–Pt*)
		e: 1x 3^{rd}(Co″–Pt*)
		f: 2x 2^{nd}(Co″–Pt*)
		g: 1x 2^{nd}(Co″–Pt*) + 1 × 3^{rd}(Co″–Pt*)

[a] Pt*: surface Pt atom; Co″: Co atoms in Co_3O_4. [b] 1^{st} (Co″–Pt*): e^- transition Co″-to-Pt*; 2^{nd} (Co″–Pt*): e^- transition Co″-to-Pt-to-Pt*; 3^{rd} (Co–Pt*): e^- transition Co″-to-2Pt-to-Pt*.

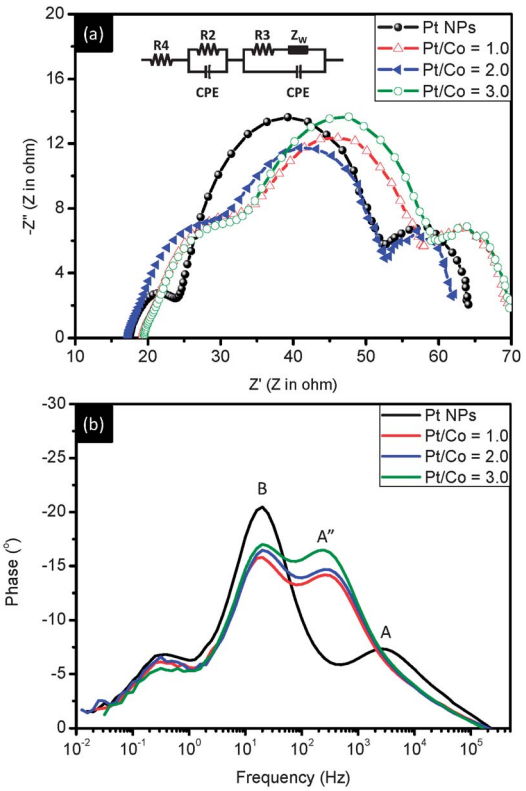

Fig. 8 Electrochemical impedance spectra of DSSCs equipped with different CNCs. (a) Nyquist plots and (b) Bode phase plot.

Table 6 Electrochemical impedance spectroscopy determined internal resistances of DSSC equipping with different CNCs

CNCs	R_2[a] (Ω)	R_3 (Ω)	R_4 (Ω)
Pt NPs	13.09	27.07	7.47
Pt/Co = 1.0	12.78	18.02	20.24
Pt/Co = 2.0	18.04	17.06	11.33
Pt/Co = 3.0	19.16	19.98	12.41

[a] R_2: the impedance at cathode/electrolyte; R_3: the impedance at TiO_2/dye/electrolyte interfaces; R_4: the impedance of Warburg diffusion process of I^-/I_3^- in the electrolyte.

dilutes the donated charge in the Pt shell region since all the CNCs of different Pt/Co ratios contain identical number of valence charge donor (Co atoms). Both the two pathways inhibit the charge transfer kinetics between Pt sites and I_3^- chemisorptions. It is important to note that the resistances of all modules are strongly correlated with each other in an electrochemical system. Therefore, the differences of R_3 and R_4 between DSSC with the four types of CNCs are expectable even the anodes with identical properties (porosity, thickness, dye loading) are applied. These differences can be explained by the surface reaction sites density (inter-particle sintering) and redox reactivity (binding energy, density of state, and the valence band structure) of the CNCs, and the corresponding charge transfer kinetics of all electrochemical modules. As shown in Table 6, the R_3 and R_4 of DSSC with Pt NPs are determined to be 27.07 Ω and 7.47 Ω, respectively. Generally, the high R_3 is attributed to the weak driving force for extracting the photo-generated electrons from I^- to the exciting state of dye at TiO_2/dye/electrolyte. On the other hand, the low R_4 refers to the efficient charge transportation in the electrolyte. Considering the charge neutralization and equilibrium in an ideal electrochemical system, the kinetics of cathodic reaction should always compatible to that of anodic ones. Herein, the high R_3 with low R_2 implies the low density of surface Pt sites for the I_3^- redox charge transportation due to the inter-particle sintering (see TEM) and the easy formation of iodide capping layers at the Pt NPs (see CV). By equipping with the C/P CNCs, the R_3 of DSSC is reduced by ~30–36% (from 27.07 Ω to 17–19 Ω) compared to that with Pt NPs. On the other hand, it increases the R_4 of DSSC by 0.66- to 1.71-folds by decreasing Pt/Co ratios from 3.0 to 1.0. Since the interparticle sintering is insignificant (see Fig. 3), one can assumes that the C/P CNCs should provide sufficient amount of reaction sites for receipting all the I_3^- anions that generated from the anodic photovoltaic reactions. In this case, the reduction of R_3 to a similar value implies the three anodes process similar redox kinetics and the slight differences of R_3 might be accounted for the marginal structure variation of individual anode. Furthermore, the increasing of R_4 is the indication for the local depletion of I^-/I_3^- redox couples due to the higher I_3^- reduction kinetics compared to the charge transportation kinetics of the electrolytes at the C/P CNCs cathode. Moreover, considering the heterogeneous catalysis mechanisms, since the R_2 of C/P CNCs is higher than that of Pt

 This journal is © The Royal Society of Chemistry 2013

Published on 19 July 2013. Downloaded by Synchrotron Radiation Library on 25/11/2013 06:52:47.

NPs the I_3^- reduction kinetic should be promoted by the increasing of surface Pt reaction sites (revealed by the suppressed interparticle sintering in Fig. 3) and the improved surface reactivity (see Fig. 6).

Further evidences on the efficient charge transportation by improving the surface reactivity of CNCs are provided by the characterization frequency peaks (across 10^{-2} to 10^5 Hz) of corresponding DSSC system in Bode phase plot (Fig. 8b). These characteristic frequency peaks can be related to as the inverse of the recombination lifetime (τ_r), or electron lifetime (τ_e) at CNCs surface.[37,38] Accordingly, it is found that the Pt NPs not only has a higher transport resistance but also has a lower electron lifetime at their surface. For DSSC with C/P CNCs cathode, the characteristic frequency peak for electron transportation on cathode (A) shifted to lower frequency (A′). This elucidates that C/P CNCs has the longer electron lifetime than Pt NPs. The prolonged lifetime of C/P CNCs reveals the increasing effective probabilities for charge transportation from surface sites of cathode to the electron/hole shuttles (I^-/I_3^-) in the electrolyte. By means of this pathway the DSSC efficient is improved. On the other hand, the peak B shifts to higher frequency position indicating the TiO_2 (or the higher charge transportation resistance) gains a shorter electron lifetime by equipping the C/P CNCs in the DSSC cathode compared to Pt NPs. The tightened electron lifetime could be attributed to the local depletion of I^-/I_3^- redox shuttles at the C/P CNCs surface region. In this case, an inverse local potential would be triggered to suppress the charge transportation (further consumption of I_3^-) at the C/P CNCs surface, and thus keeping the charge neutralization in an electrochemical system. This local depletion is also the cause for the reduction of DSSC onset potential. As clearly shown in Table 6, the cathode with Pt/Co = 1.0 gains the highest R_4 among cathode with rest of CNCs. It implying that the C/P CNCs generates the highest extent of local depletion (the strongest inverse potential) and thus resulting in the lowest V_{OC} of DSSC among the experiment CNCs.

Conclusions

In summary, we synthesized the NPs comprising of a Co_3O_4 core crystallite and the Pt shell crystallite with varied thicknesses as cathodic electrocatalyst in DSSC. Our structural analyses together with the photovoltaic characterizations elucidate that the Co core would slightly lower the d-band level and increases the valence band DOS of surface Pt *via* inducing the expansive strain at shell region. By these interactions, the Co atoms would inject valence charge to the Pt shell atoms. We found that such lattice strain induced heteroatomic interaction facilitates the I_3^- to I^- reduction at C/P CNCs cathode. Compared to a DSSC with Pt NPs cathode, the C/P CNCs cathode in DSCs improves the J_{SC} by 22.9% (from 11.01 to 13.53 mA cm^{-2}); consequently meliorate the η by ~36.2% (from 4.41 to 6.01%). Besides, the proposed strategy in this study enables an approximately 90% or higher Pt utilization and 61% reduction in the amount of Pt metal when compared to the cathode with Pt NPs. Furthermore, the catalytic activity of the core–shell NPs is tuneable by changing the shell thickness and the core configurations. Most importantly, our full scope structural characterizations combining with the photovoltaic analysis have outlined the necessary relationship between structure and heterogeneous surface to improve the design of future excitonic solar cells.

Acknowledgements

The authors would like to thank the staff of National Synchrotron Radiation Research Center (NSRRC), Hsinchu, Taiwan for the help in various synchrotron-based measurements techniques. A special thank is due to Prof. Shih-Yuan Lu and his research group (Dept. of Chemical Engineering, NTHU) who helped to analyse the CV data. T.-L. Lin and T.-Y. Chen acknowledge the financial supports from National Science Council, project no. NSC 99-2113-M-007-014-MY3 (T.-L. Lin). We would also like to thank the support of the research grant of National Tsing Hua University, Grant no. 102N2012E1. C.-H. Lee acknowledges the financial support from the National Science Council project: NSC99-2923-M007-004-MY3.

Notes and references

1 G. Calogero, P. Calandra, A. Irrera, A. Sinopoli, I. D. Citro and G. Marco, *Energy Environ. Sci.*, 2011, **4**, 1838–1844.
2 G. Boschloo and A. Hagfeldt, *Acc. Chem. Res.*, 2009, **42**, 1819–1826.
3 G.-R. Li, F. Wang, Q.-W. Jiang, X.-P. Gao and P.-W. Shen, *Angew. Chem., Int. Ed.*, 2010, **49**, 3653–3656.
4 M. X. Wu, X. Lin, A. Hagfeldt and T. L. Ma, *Angew. Chem.*, 2011, **123**, 3582–3586.
5 M. Graetzel, R. A. J. Janssen, D. B. Mitzi and E. H. Sargent, *Nature*, 2012, **488**, 304–312.
6 P. Calandra, G. Calogero, A. Sinopoli and P. G. Gucciardi, *Int. J. Photoenergy*, 2010, **2010**, 109495.
7 L. Wang, M. X. Wu, Y. R. Gao and T. L. Ma, *Appl. Phys. Lett.*, 2011, **98**, 221102.
8 K. Sasaki, H. Naohara, Y. Cai, Y. M. Chio, P. Liu, M. B. Vukmirovic, J. X. Wang and R. R. Adzic, *Angew. Chem., Int. Ed.*, 2010, **49**, 8602–8607.
9 A. Kay and M. Grätzel, *Sol. Energy Mater. Sol. Cells*, 1996, **44**, 99–117.
10 M. K. Wang, A. M. Anghel, B. Marsan, N. C. Ha, N. Pootrakulchote, S. M. Zakeeruddin and M. Grätzel, *J. Am. Chem. Soc.*, 2009, **131**, 15976–15977.
11 M. Wu, X. Lin, Y. Wang, L. Wang, W. Guo, D. Qi, X. Peng, A. Hagfeldt, M. Grätzel and T. Ma, *J. Am. Chem. Soc.*, 2012, **134**, 3419–3428.
12 O. A. Ileperuma, M. A. K. L. Dissanayake and S. Somasundaram, *Electrochim. Acta*, 2002, **47**, 2801–2807.
13 M. Watanabe and S. Motoo, *J. Electroanal. Chem.*, 1975, **60**, 275–283.
14 T. Bligaard and J. K. Nørskov, *Electrochim. Acta*, 2007, **52**, 5512–5516.
15 P. Strasser, S. Koh, T. Anniyev, J. Greeley, K. More, C. Yu, Z. Liu, S. Kaya, D. Nordlund, H. Ogasawara, M. F. Toney and A. Nilsson, *Nat. Chem.*, 2010, **2**, 454–460.
16 S. Alayoglu, A. U. Nilekar, M. Mavrikakis and B. Eichhorn, *Nat. Mater.*, 2008, **7**, 333–338.

Published on 19 July 2013. Downloaded by Synchrotron Radiation Library on 25/11/2013 06:52:47.

17 A. Schlapka, M. Lischka, A. Gross, U. Kasberger and P. Jakob, *Phys. Rev. Lett.*, 2003, **91**, 016101.
18 R. R. Adzic, J. Zhang, K. Sasaki, M. B. Vukmirovic, M. Shao, J. X. Wang, A. U. Nilekar, M. Mavrikakis, J. A. Valerio and F. Uribe, *Top. Catal.*, 2007, **46**, 249–262.
19 R. R. Adzic, J. Zhang, K. Sasaki, M. B. Vukmirovic, M. Shao, J. X. Wang, A. U. Nilekar, M. Mavrikakis, J. A. Valerio and F. Uribe, *Nano Res.*, 2009, **2**, 406–415.
20 T.-Y. Chen, T.-L. Lin, T.-J. M. Luo, Y. Chio and J.-F. Lee, *ChemPhysChem*, 2010, **11**, 2383–2392.
21 T.-Y. Chen, I.-L. Chen, Y.-T. Liu, T.-L. Lin, P.-W. Yang, C.-Y. Wu, C.-C. Hu, T.-J. M. Luo and C.-H. Lee, *CrystEngComm*, 2013, **15**, 982–994.
22 T.-Y. Chen, T.-J. M. Luo, Y.-W. Yang, Y.-C. Wei, K.-W. Wang, T.-L. Lin, T.-C. Wen and C.-H. Lee, *J. Phys. Chem. C*, 2012, **116**, 16969–16978.
23 R. R. Adzic, J. Zhang, K. Sasaki, M. B. Vukmirovic, M. Shao, J. X. Wang, A. U. Nilekar, M. Mavrikakis, J. A. Valerio and F. Uribe, *Top. Catal.*, 2007, **46**, 249–262.
24 M. P. Hogarth and T. R. Ralph, *Platinum Met. Rev.*, 2002, **46**, 117–135.
25 J. Teixeira, *J. Appl. Crystallogr.*, 1988, **21**, 781–785.
26 J. Wagner, *J. Appl. Crystallogr.*, 2004, **37**, 750–756.
27 T.-Y. Chen, T.-J. M. Luo, Y.-W. Yang, Y.-C. Wei, K.-W. Wang, T.-L. Lin, T.-C. Wen and C.-H. Lee, *J. Phys. Chem. C*, 2012, **116**, 16969–16978.
28 T.-Y. Chen, I.-L. Chen, Y.-T. Liu, T.-L. Lin, P.-W. Yang, C.-Y. Wu, C.-C. Hu, T.-J. M. Luo and C.-H. Lee, *CrystEngComm*, 2013, **15**, 982–994.
29 M. Zinke-Allmang, L. C. Feldman and M. H. Grabow, *Surf. Sci. Rep.*, 1992, **16**, 377–463.
30 F. Besenbacher, I. Chorkendorff, B. S. Clausen, B. Hammer, A. M. Molenbroek, J. K. Nørskov and I. Stensgaard, *Science*, 1998, **279**, 1913–1915.
31 S. N. Reifsnyder, M. M. Otten, D. E. Sayers and H. H. Lamb, *J. Phys. Chem. B*, 1997, **101**, 4972–4977.
32 A. N. Mansour, J. W. Cook and D. E. Sayers, *J. Phys. Chem.*, 1984, **88**, 2330.
33 B. J. Hwang, S. M. S. Kumar, C. H. Chen, R. W. Chang, D. G. Liu and J. F. Lee, *J. Phys. Chem. C*, 2008, **112**, 2370–2377.
34 P. J. Godowski, Z. S. Li, J. Bork and J. Onsgaard, *Surf. Rev. Lett.*, 2007, **14**, 911–914.
35 T.-Y. Chen, T.-J. M. Luo, Y.-W. Yang, Y.-C. Wei, K.-W. Wang, T.-L. Lin, T.-C. Wen and C.-H. Lee, *J. Phys. Chem. C*, 2012, **116**, 16969–16978.
36 J. D. Newson and A. C. Riddiford, *J. Electrochem. Soc.*, 1961, **108**, 699–706.
37 G. Schlichthorl, S. Y. Huang, J. Sprague and A. J. Frank, *J. Phys. Chem. B*, 1997, **101**, 8141–8155.
38 G. Schlichthorl, N. G. Park and A. J. Frank, *J. Phys. Chem. B*, 1999, **103**, 782–791.

 This journal is © The Royal Society of Chemistry 2013